

Simultaneously improving piezoelectric properties and temperature stability of $\text{Na}_{0.5}\text{K}_{0.5}\text{NbO}_3$ (KNN)-based ceramics sintered in reducing atmosphere

Zhenyong CEN^a, Shuaishuai BIAN^a, Ze XU^a, Ke WANG^a,
Limin GUO^b, Longtu LI^a, Xiaohui WANG^{a,*}

^aState Key Laboratory of New Ceramics and Fine Processing, School of Materials
Science and Engineering, Tsinghua University, Beijing 100084, China

^bSchool of Science, Beijing University of Posts and Telecommunications, Beijing 100876, China

Received: January 11, 2021; Revised: February 20, 2021; Accepted: March 10, 2021

© The Author(s) 2021.

Abstract: It is a very difficult work to sinter $\text{K}_{0.5}\text{Na}_{0.5}\text{NbO}_3$ (KNN)-based materials with good reduction resistance in strong reducing atmosphere. $0.945\text{K}_{0.48}\text{Na}_{0.52}\text{Nb}_{0.96}\text{Ta}_{0.04}\text{O}_3-0.055\text{BaZrO}_3 + 0.03\text{ZrO}_2 + y \text{ mol}\% \text{MnO}$ (KNNT–0.055BZ + 0.03Zr + yMn) ceramics sintered in reducing atmosphere were prepared successfully by conventional solid-state reaction methods. MnO dopant increases grain size at $y = 5-8$ due to strong lattice distortion and then decreases grain size at $y = 9$ due to much $\text{Mn}_4\text{Nb}_2\text{O}_9$ accumulated at the grain boundary. MnO dopant as an excellent sintering aid can effectively reduce volatilization of alkali metal by decreasing the sintering temperature (T_{sinter}). Reducing alkali metal volatilization can greatly reduce oxygen vacancies and improve piezoelectric properties. MnO dopant can improve the anti-reduction properties. The KNNT–0.055BZ + 0.03Zr + yMn ceramics at $y = 6-9$ show outstanding anti-fatigue of unipolar piezoelectric strain under the synergistic effect of reduced oxygen vacancies due to reduced volatilization and increased grain size. Piezoelectric properties and temperature stability of KNNT–0.055BZ + 0.03Zr ceramics sintered in reducing atmosphere are improved simultaneously by MnO dopant. Optimum inverse piezoelectric coefficient (d_{33}^*) of ceramics at $y = 8$ reaches up to 480 pm/V under low driving electric field $E = 20 \text{ kV/cm}$ at room temperature, and its temperature stability of d_{33}^* reaches 158 °C. It will be an excellent lead-free material candidate for the preparation of multilayer piezoelectric actuators co-fired with nickel electrode.

Keywords: lead-free piezoelectric ceramics; reducing atmosphere; fatigue property; temperature stability

1 Introduction

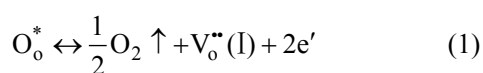
A great deal of attention for the lead-free piezoelectric materials was recently given to the $\text{Na}_{0.5}\text{K}_{0.5}\text{NbO}_3$

(KNN)-based ceramics due to the excellent piezoelectric properties and environmental friendliness [1]. The KNN-based ceramics are considered to be one of the most promising lead-free systems to replace lead-based ceramics. However, a gap of piezoelectric properties between lead-free systems and lead-based systems still exists. In the application of piezoelectric actuator, it is

* Corresponding author.
E-mail: wxh@tsinghua.edu.cn

possible that a KNN-based multilayer can obtain a displacement comparable to that of lead-based ceramics by stacking more ceramic layers with smaller thickness [2]. The multilayer design of piezoelectric materials brings great hope for the application of lead-free piezoelectric materials. It means that multilayer structure design can make up for the lack of piezoelectric strain for KNN-based ceramics. Inner electrode of multilayer piezoelectric actuator is usually a costly silver palladium electrode. It can greatly reduce the cost of device by using base metal electrode (e.g., nickel electrode and copper electrode). KNN-based materials must be sintered in reducing atmosphere, because the co-fired base metal electrode is easily oxidized in air. Here, KNN-based materials with excellent anti-reduction properties and piezoelectric properties would be selected to investigate.

High oxygen vacancy concentration would result in deterioration of piezoelectric properties for KNN-based ceramics [3,4]. Many sources of oxygen vacancies exist in KNN-based ceramics sintered in reducing atmosphere. Oxygen ions escape from the perovskite structure induced by reducing atmosphere, as shown in the following equation. This kind of oxygen vacancy is marked as $V_o^{**}(I)$.



When KNN-based ceramics are sintered in high temperatures, the irreversible volatilization of alkali metals can also result in the formation of oxygen vacancy (marked as $V_o^{**}(II)$). In addition, some oxygen vacancies (marked as $V_o^{**}(III)$) are produced due to the acceptor doping. In KNN-based ceramics, the oxygen vacancies will affect fatigue properties, temperature stability, and piezoelectric properties.

Although A-site vacancy (V_A') can interact with spontaneous polarization (P_s) inside each domain, which results in giant electric-field-induced strains [5]. It is difficult to control the A-site vacancy concentration due to the poor sinterability of KNN-based ceramics and sintering environment fluctuation. The activation energy (about 4 eV) of the A-site cation migration is lower than that (around 14 eV) of B-site cation transport in ABO_3 perovskite materials [6,7]. It suggests that defects in B-site should be more stable than defects in A-site. Moreover, the associated weak dipole defects ($V_o^{**} - V_{Na}'$, $V_o^{**} - V_K'$) could easily dissociate [8]. Thus, we consider that the dipole defects associated with B-site defects and oxygen vacancy should be more

stable. Decrease of the sintering temperature (T_{sinter}) can effectively reduce V_A' concentration, which can decrease oxygen vacancies ($V_o^{**}(II)$) in ceramics. Manganese oxide as a good sintering aid is used to decrease the T_{sinter} and increase density [9–11]. However, for KNN-based ceramics, Mn ions usually substitute for the ions in B-site to form oxygen vacancy ($V_o^{**}(III)$) [12,13]. Because of the stability of dipole defects in B-site, we believe that Mn ion doping is very likely to control or decrease the oxygen vacancy in ceramics, improving the fatigue properties, temperature stability, and piezoelectric properties.

In this work, the fatigue properties, temperature stability, and piezoelectric properties of MnO doped $0.945K_{0.48}Na_{0.52}Nb_{0.96}Ta_{0.04}O_3-0.055BaZrO_3 + 0.03ZrO_2$ (KNNT–0.055BZ + 0.03Zr) ceramics are investigated systematically. Optimum inverse piezoelectric coefficient (d_{33}^*) of ceramics at $y = 8$ reaches up to 480 pm/V under low driving electric field $E = 20$ kV/cm at room temperature, and its temperature stability of d_{33}^* reaches 158 °C. The KNNT–0.055BZ + 0.03Zr + y Mn (y Mn: y mol% MnO) ceramics at $y = 6-9$ show outstanding anti-fatigue of unipolar piezoelectric strain ($\beta > 94\%$) under the synergistic effect of reduced oxygen vacancies due to reduced volatilization and increased grain size.

2 Experimental

Lead-free KNNT–0.055BZ + 0.03Zr + y Mn ($y = 5, 6, 7, 8,$ and 9) piezoelectric ceramics were prepared by conventional solid-state reaction method. Non-stoichiometric 0.03 mol ZrO_2 is co-doped in the $0.945K_{0.48}Na_{0.52}Nb_{0.96}Ta_{0.04}O_3-0.055BaZrO_3$ system to improve its anti-reduction properties [14]. Powders of $BaCO_3$, Nb_2O_5 , Na_2CO_3 , K_2CO_3 , ZrO_2 , $MnCO_3$, and Ta_2O_5 (analytically pure) were weighed out. The powders were milled using a planetary ball-milling method with zirconia balls and ethanol for 24 h. After drying at 70 °C, the powders were calcined at 850 °C for 5 h in air. The calcined powders were again milled and then compacted into pellets with the diameter of 8 mm and the thickness of 1 mm by uniaxial pressing in a stainless-steel die using polyvinyl Butyralas binder. The green pellets were placed in a muffle furnace to remove the binder at 600 °C for 2 h and in air. After removing the binder, the green pellets were fired at a heating rate of 5 °C/min to 1060–1105 °C and held for

2 h in reducing atmosphere (H_2/N_2 : oxygen partial pressure (p_{O_2}) range of 10^{-12} – 10^{-11} MPa). After cooling to 850 °C, the reducing atmosphere was artificially regulated to be p_{O_2} range of 10^{-8} – 10^{-7} MPa and held for 6–8 h. Then, the atmosphere condition was kept and cooled naturally. Figure S1 in the Electronic Supplementary Material (ESM) provides photos of KNNT–0.055BZ + 0.03Zr + y Mn ceramics at $y = 0$ –4. KNNT–0.055BZ + 0.03Zr + y Mn green pellets at $y = 0$ –1 cannot be sintered into ceramics so it cannot be measured and KNNT–0.055BZ + 0.03Zr + y Mn sintered samples at $y = 2$ –4 cannot be measured difficultly due to the serious semiconductive behavior.

Crystal structure of samples was characterized using the X-ray diffraction (XRD) (Rigaku 2500, Rigaku, Japan). Surface microstructures of the ceramics after simple artificial polishing and thermal etching at 1050–1000 °C for 30 min were measured with a scanning electron microscope (SEM, MERLIN VP Compact, Zeiss Ltd., Germany). The ion sputtering equipment (SBC-12, KYKY Technology Co., China) was used to sputter gold electrodes. The samples were poled in a silicone oil bath under a DC field of 3 kV/mm and 100 °C for 30 min. The quasistatic piezoelectric coefficient (d_{33}) was measured approximately 2 days after poling using a Berlincourt d_{33} meter (ZJ-6A; Institute of Acoustics, Chinese Academy of Sciences, China). Room-temperature piezoelectric and dielectric properties were determined by an impedance analyzer (Agilent 4294A; Agilent, Santa Clara, CA, USA). The temperature-dependent dielectric properties at 1 kHz were measured using a capacitance meter (HP4278A; Hewlett-Packard, USA) at (–80)–350 °C with a temperature-controlled microscope stage (TLRS-003, Tongguo Technology, China). The electric-field-induced strain (S – E) curves in the temperature range from 25 to ~180 °C were measured *in situ* using the TF Analyzer 2000E ferroelectric measuring system (aixACCT Systems GmbH, Aachen, Germany). The unipolar fatigue cycles of ceramics were done by a high-voltage power amplifier test with the programmatic system (Model 10/40A, TREK INC, USA). The ceramics were fatigued with a unipolar triangle electric signal with the amplitude of 20 kV/cm

at 10 Hz up to 1×10^6 cycles and were measured at 20 kV/cm at 1 Hz by using the TF Analyzer 2000E ferroelectric measuring system. The X-ray photoelectron spectra (XPS) of Mn ions for samples were obtained to characterize their valence state using the X-ray photoelectron microprobe (ESCALAB 250Xi, Thermofisher, UK) equipped with a standard monochromatic Al K α excitation source ($h\nu = 1361$ eV).

3 Results and discussion

Similar density values of ceramics are obtained via controlling the T_{sinter} . Table 1 lists the densities (ρ) of KNNT–0.055BZ + 0.03Zr + y Mn ceramics sintered in different temperatures. The ρ of each component is 4.571, 4.569, 4.568, 4.566, and 4.561 $g \cdot cm^{-3}$, respectively. In Table 1, at $y = 5$ –8, the T_{sinter} of samples with an approximate density value decreases gradually from 1105 to 1060 °C due to the MnO doping. It confirms that the MnO dopant as a good sintering aid can reduce effectively T_{sinter} at $y = 5$ –8. However, for ceramics at $y = 9$, the approximate density can be obtained only when its T_{sinter} is increased to 1070 °C. It indicates that adding more MnO content cannot reduce the T_{sinter} all the time. It is related to the appearance of the second phase. Simultaneously, the sintering temperature differences (ΔT) between adjacent components are listed in Table 1. In detail, the ΔT decreases from 20 to 10 °C, which suggests the effect of MnO as a sintering aid is weakening and the negative value (–10 °C) of ΔT finally appears at $y = 9$. It can be firmly believed that the decrease of T_{sinter} would decrease the amount of alkali metal volatilization.

Figure 1(a) shows SEM microphotographs of KNNT–0.055BZ + 0.03Zr + y Mn ceramics. In Fig. 1, it can be observed that the grain size changes obviously due to the MnO doping. The grain size distribution of KNNT–0.055BZ + 0.03Zr + y Mn ceramics is shown in Fig. 1(b). MnO doping induces the average grain size to increase from 1.02 to 1.65 μm at $y = 5$ –8 and then decrease to 1.11 μm at $y = 9$. The ceramics at $y = 8$ have the largest average grain size (1.65 μm). In Table 1, the

Table 1 ρ and ΔT between adjacent components for KNNT–0.055BZ + 0.03Zr + y Mn ceramics sintered in different temperatures

	$y = 5$	$y = 6$	$y = 7$	$y = 8$	$y = 9$
T_{sinter} (°C)	1105	1085	1070	1060	1070
ΔT (°C)		$\Delta T_{5-6} = 20$	$\Delta T_{6-7} = 15$	$\Delta T_{7-8} = 10$	$\Delta T_{8-9} = -10$
ρ ($g \cdot cm^{-3}$)	~4.571	~4.569	~4.568	~4.566	~4.561

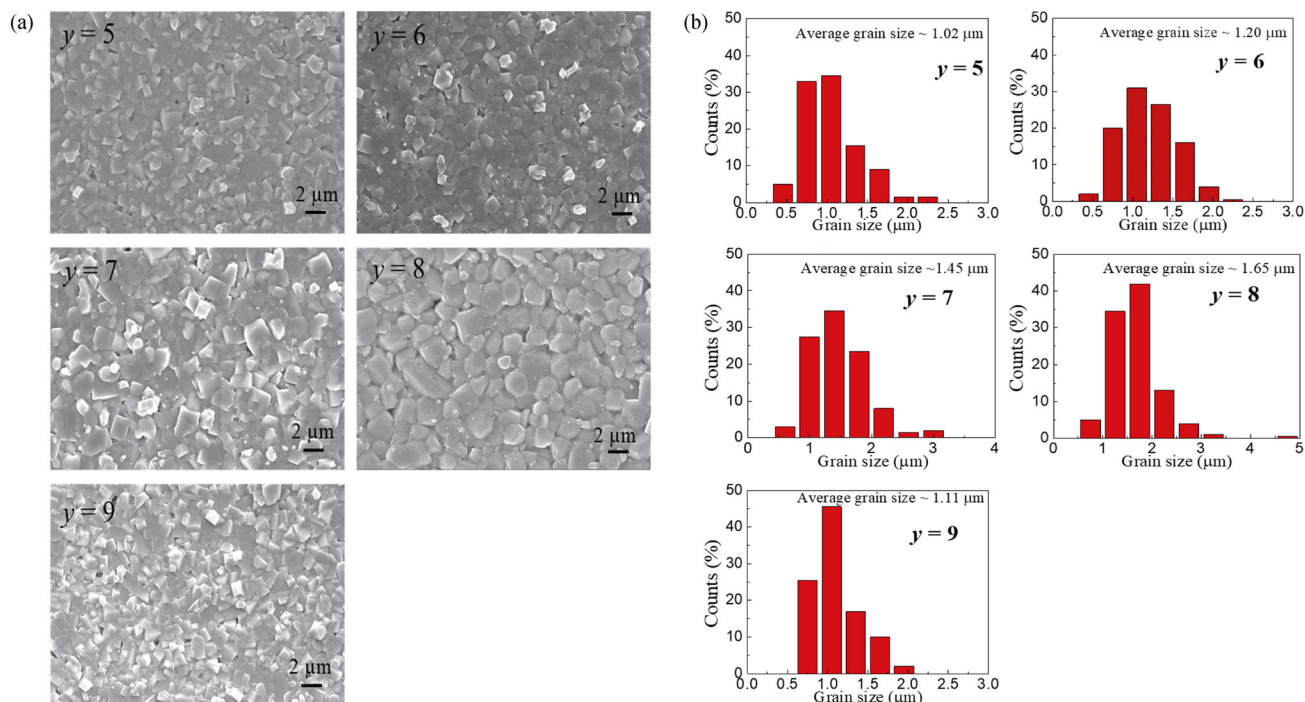


Fig. 1 (a) SEM microphotographs and (b) grain size distributions of KNNT–0.055BZ + 0.03Zr + *y*Mn ceramics.

T_{sinter} of ceramics with approximate density values can be decreased from 1105 to 1060 °C. It can be found that the T_{sinter} of the sample reduces, but the grain size of the sample still increases. We consider that the B-site substitution of Mn ions causes strong lattice distortion, which accelerates the sintering. When *y* reaches to 9, the grain size of ceramics decreases to 1.11 μm. A large number of second phase ($Mn_4Nb_2O_9$) are accumulated at the grain boundary as shown in Fig. 2. $Mn_4Nb_2O_9$ hinders the grain boundary migration and leads to the decrease of grain size.

Figure 2(a) shows XRD patterns of KNNT–0.06BZ + 0.03Zr + *y*Mn ceramics at $2\theta = 20^\circ\text{--}65^\circ$. All ceramics show perovskite structure. Ceramics at *y* = 5 show an additional phase (Mn_3O_4). When *y* increases from 6 to 9, Mn_3O_4 disappears and ZrO_2 exists stably. In addition,

$Mn_4Nb_2O_9$ appears and increases gradually at *y* = 6–9. Figure 2(b) reveals the XRD patterns of KNNT–0.06BZ + 0.03Zr + *y*Mn ceramics at $2\theta = 44^\circ\text{--}52^\circ$. All ceramics possess R phase that is consistent with Ref. [19], which suggests that MnO dopant does not induce phase transition.

Figure 3(a) shows XPS of Mn 2p for KNNT–0.055BZ + 0.03Zr + *y*Mn ceramics. The first peak at ~640.62 eV, the second peak at ~641.60 eV, and the third peak at ~642.64 eV correspond to Mn^{2+} , Mn^{3+} , and Mn^{4+} ions, respectively [15]. In Fig. 3, the Mn ions of KNNT–0.055BZ + 0.03Zr + *y*Mn ceramics show different valence states. At *y* = 5, three valence states (+2, +3, and +4) of Mn ions exist in ceramics. When *y* increases from 6 to 9, the Mn^{3+} ions in ceramics disappear and two valence states (+2, +4) of Mn ions exist in ceramics. Table S1 in the ESM lists the surface area under the peak located at ~640.62, ~641.60, and ~642.62 eV of Mn 2p in KNNT–0.055BZ + 0.03Zr + *y*Mn ceramics. The ratio under the peak located at ~640.62 (Mn^{2+}), ~641.60 (Mn^{3+}), and ~642.62 eV (Mn^{4+}) of Mn 2p of KNNT–0.055BZ + 0.03Zr + *y*Mn ceramics is shown in Fig. 3(f). When increasing *y* from 5 to 8, the ratio of Mn^{2+} ions increases from 77.05% to 91.04% and the ratio of Mn^{4+} ions decreases from 19.05% to 8.86%. However, the ratio of Mn^{2+} ions decreases and the ratio of Mn^{4+} ions increases in the ceramics at *y* = 9.

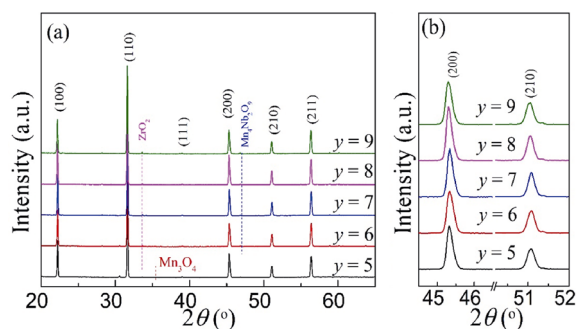


Fig. 2 XRD patterns of KNNT–0.055BZ + 0.03Zr + *y*Mn ceramics: (a) $2\theta = 20^\circ\text{--}65^\circ$ and (b) $2\theta = 44^\circ\text{--}52^\circ$.

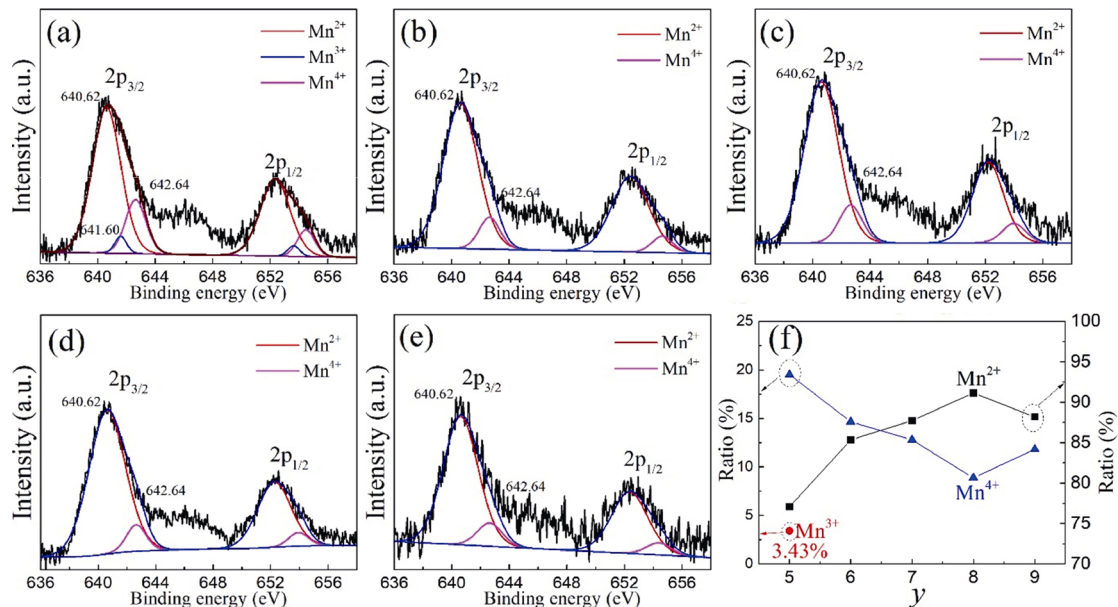
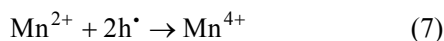
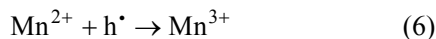
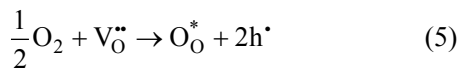
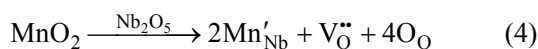
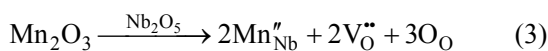
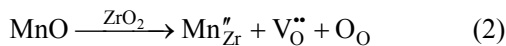


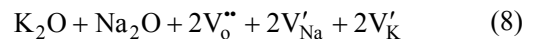
Fig. 3 XPS of Mn 2p for KNNT–0.055BZ + 0.03Zr + *y*Mn ceramics: (a) *y* = 5, (b) *y* = 6, (c) *y* = 7, (d) *y* = 8, and (e) *y* = 9. (f) The ratios under the peaks located at ~640.62 (Mn²⁺), ~641.60 (Mn³⁺), and ~642.62 eV (Mn⁴⁺) of Mn 2p of KNNT–0.055BZ + 0.03Zr + *y*Mn ceramics.

When *y* increases from 5 to 9, more Mn enters B-site. By comparing the ionic radii of Mn²⁺(0.83 Å:6CN)/Mn³⁺(0.645 Å:6CN)/Mn⁴⁺(0.53 Å:6CN) with Nb⁵⁺(0.64 Å:6CN)/Zr(0.72 Å:6CN) (CN is the coordination number), Mn ions substitute for Zr⁴⁺ ions and Nb⁵⁺ ions in B-site as shown in Eqs. (2)–(4) due to the similar ionic radius [16,17]. In ceramics, the Mn ions with high valence state form due to the re-oxidation of oxygen vacancy as shown in Eq. (5). The holes (h[•]) are absorbed by Mn²⁺ ions as shown in Eqs. (6) and (7).



The total ratio of Mn ions (Mn³⁺ and Mn⁴⁺) with high valence state decreases with increasing *y* from 5 to 8. It suggests that the oxygen vacancy concentration that can be re-oxidized is reduced. It may imply the oxygen vacancy concentration in KNNT–0.055BZ + 0.03Zr + *y*Mn ceramics should be reduced at *y* = 5–8. As previously analyzed, the Mn ions substitute for Zr⁴⁺

and Nb⁵⁺ ions in B-site to form oxygen vacancies. This does not contradict the current results. Decreases of *T*_{sinter} can reduce the content of alkali metal volatilization [18]. Some oxygen vacancies are from irreversible alkali metal volatilization as shown in Eq. (8). Here, the decrease of *T*_{sinter} for KNNT–0.055BZ + 0.03Zr + *y*Mn ceramics will reduce alkali metal volatilization.



At *y* = 5–8, the effect of *T*_{sinter} on oxygen vacancy concentration should be stronger than that of Mn ions substitution.

However, the ratio of Mn⁴⁺ ions for ceramics at *y* = 9 increases to 11.82%. It attributes to the increase of *T*_{sinter}. High *T*_{sinter} (1070 °C) leads to the increase of alkali metal volatilization. Thus, in the ceramics at *y* = 9, hole from re-oxidation increases, which results in the increase of Mn⁴⁺ ion ratio. In summary, we consider that the oxygen vacancy concentration in ceramics should decrease first at *y* = 5–8 and then increase at *y* = 9. Therefore, oxygen vacancies caused by the volatilization of alkali metals account for a large proportion of oxygen vacancies in the materials. The oxygen vacancy concentration in ceramics should decrease first at *y* = 5–8 and then increase at *y* = 9.

Figure S2 in the ESM shows impedance spectroscopy for KNNT–0.055BZ + 0.03Zr + *y*Mn ceramics measured at different temperatures. The impedance spectroscopies

are fitted via Zview software by an equivalent electrical circuit comprising of two RC circuits (R parallel to C) connected in series. The equivalent electrical circuit of KNNT–0.055BZ + 0.03Zr + yMn ceramics is shown in Fig. 4. Two RC circuits are grain boundary and grain, respectively.

Table 2 shows activation energy of grain boundary (E_{gb}), activation energy of grain (E_g), and difference (ΔE) between E_{gb} and E_g for KNNT–0.055BZ + 0.03Zr + yMn ceramics. It can be observed that at $y = 5-9$, the E_{gb} is higher than E_g , which is due to the Schottky barrier in the grain boundary. For BaTiO₃-based thermosensitive ceramics sintered in reducing atmosphere, it is difficult to establish Schottky barrier at grain boundary, because grain and grain boundary both are semiconductive [20,21]. Ceramics must be re-oxidized to establish Schottky barrier in the grain boundary [21,22]. Here, the ceramics are re-oxidized in the atmosphere ($p_{O_2} = 10^{-8}-10^{-7}$ MPa). Thus, Schottky barrier is established in the grain boundary. In Table 2, the E_{gb} and E_g both increase first at $y = 5-8$ and then decrease at $y = 9$. E_{gb} and E_g reach the maximum values (0.80 and 0.76 eV, respectively). This confirms the previous results on the change of oxygen vacancy concentration. We consider that ceramics at $y = 8$ should have the lowest oxygen vacancy concentration. In the regulation of oxygen vacancies in KNN-based ceramics, the effect of reducing T_{sinter} is stronger than that of Mn ion substitution in B-site.

Oxygen vacancies need to overcome additional energy to pass grain boundary due to the Schottky barrier in grain boundary [23]. We consider that the difference (ΔE) between E_{gb} and E_g should reflect the height of Schottky barrier. Table 2 lists the ΔE of KNNT–0.055BZ + 0.03Zr + yMn ceramics. It can be

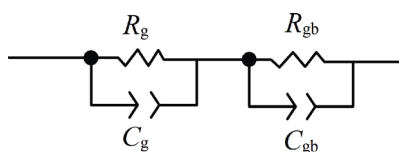


Fig. 4 An equivalent electrical circuit of KNNT–0.055BZ + 0.03Zr + yMn ceramics.

Table 2 Activation energy of E_{gb} , E_g , and ΔE between E_{gb} and E_g for KNNT–0.055BZ + 0.03Zr + yMn ceramics

Activation energy	y = 5	y = 6	y = 7	y = 8	y = 9
E_{gb} (eV)	0.74	0.78	0.79	0.80	0.79
E_g (eV)	0.66	0.71	0.73	0.76	0.72
ΔE (eV)	0.08	0.07	0.06	0.04	0.07

observed that the ΔE decreases from 0.08 to 0.04 eV and then increases to 0.07 eV. The ΔE of ceramics at $y = 8$ shows the minimum value (0.04 eV). It should possess minimum Schottky barrier height. The decrease of grain size is beneficial to the increase of Schottky barrier [24]. In Fig. 1, it can be observed that the ceramics at $y = 8$ have the maximal grain size (1.68 μm). It corresponds to the minimum ΔE value. Thus, ceramics with fine grain have a high Schottky barrier.

Figure 5(a) shows insulation resistivity (k) of KNNT–0.055BZ + 0.03Zr + yMn ceramics. The MnO dopant can improve the k of KNNT–0.055BZ + 0.03Zr + yMn ceramics. The ceramics at $y = 8$ show an optimum k ($7.74 \times 10^{11} \Omega \cdot \text{cm}$). MnO can effectively improve the reduction resistance of the KNNT–0.055BZ + 0.03Zr + yMn ceramics. Figure 5(b) shows the dielectric constant (ϵ_r) and dielectric loss ($\tan\delta$) measured at 1 kHz for KNNT–0.055BZ + 0.03Zr + yMn ceramics at the temperature range of $(-80)-350$ °C. It can be observed that the Curie temperature (T_c) of ceramics at $y = 5-9$ is around ~ 200 °C. In Fig. 5(b), $\tan\delta$ at one temperature point (T_i) sharply increase. Thermally activated defects and space charges would overcome the potential barrier to be with increasing operation temperature, which results in a large loss form [25]. In Fig. 5(b), it can be observed that the T_i corresponding to the sharp increase of $\tan\delta$ moves to high temperatures at $y = 5-8$. It has been confirmed that oxygen vacancies decrease gradually at $y = 5-8$ and then increase at $y = 9$. The low oxygen vacancy concentration should be the reason for the T_i moving to high temperatures. The T_i of ceramics at $y = 9$ moves to low temperatures, which attributes to the decrease of oxygen vacancy concentration. Figure 5(c) shows ferroelectric hysteresis loop ($P-E$) of KNNT–0.055BZ + 0.03Zr + yMn ceramics at the frequency of 1 Hz under 30 kV/cm. The ceramic at $y = 5$ shows an obvious “Nod” behavior due to the high oxygen vacancy migration under $E = 30$ kV/cm. The movable oxygen vacancies under the electric field contribute to the conductivity, which leads to the inaccuracy of the $P-E$ loop [26]. In Fig. 5(c), the ceramics at $y = 6-9$ do not show “Nod” behavior, which suggests that the mobile oxygen vacancy concentration under the applied electric field is relatively low.

Figure 5(d) shows bipolar strain–electric ($S-E$) curves of KNNT–0.055BZ + 0.03Zr + yMn ceramics at the frequency of 1 Hz under 30 kV/cm. The P_s could be switched toward the direction of the applied electric field to generate an electro-strain due to the switch and

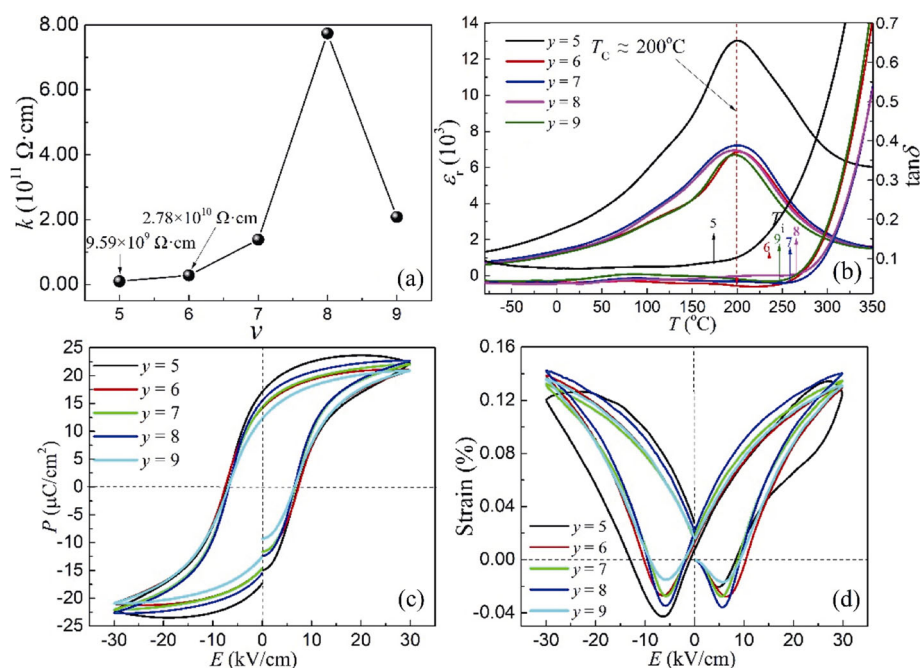


Fig. 5 (a) k of KNNT-0.055BZ + 0.03Zr + y Mn ceramics. (b) ϵ_r and $\tan \delta$ measured at 1 kHz for KNNT-0.055BZ + 0.03Zr + y Mn ceramics at the temperature range of (-80) – 350°C . (c) P - E loop and (d) S - E curves of KNNT-0.055BZ + 0.03Zr + y Mn ceramics at the frequency of 1 Hz under 30 kV/cm.

extension of P_s [27,28]. However, an interaction between defects and P_s inside domains occurs [29]. We consider that the movable oxygen vacancies with high concentration in the ceramics at $y = 5$ should disturb P_s inside domains. Thus, the S - E curves of ceramics at $y = 5$ are very asymmetric. At $y \geq 6$, the symmetry of S - E curves becomes high, because the oxygen vacancy concentrations in ceramics at $y = 6$ – 9 are lower than that of ceramics at $y = 5$. In Fig. 5(d), it can be observed that the positive strain (S_{pos}) can be improved due to the MnO dopant at $y = 5$ – 8 . The S_{pos} consists of intrinsic piezoelectric response strain (S_{piezo}) and extrinsic domain switching strain (S_{switch}). In Fig. 2(b), phases of all ceramics are R phase, which suggests the S_{piezo} from intrinsic contribution in all ceramics should be similar. Thus, the change of S_{pos} should be attributed to the S_{switch} . The S_{switch} belongs to extrinsic contribution and is influenced by other extrinsic factors (e.g., grain size, defects, internal stress, and domain size, etc.). In Fig. 1, average grain size increases at $y = 5$ – 8 , and decreases at $y = 9$. The increase of grain size can result in the decrease of internal stress, which is beneficial to the domain switching. More non- 180° domains are retained after removing the electric field. Those non- 180° domains become irreversible. A large number of irreversible domain formation corresponds to the decrease of negative strain (S_{neg}) and increase of d_{33}

[30]. Simultaneously, the oxygen vacancy concentration decreases gradually, at $y = 5$ – 8 , which weakens the pinning effect for domains. When y reaches to 9, the S_{pos} decreases to 0.13%. The internal stress and increase of oxygen vacancy concentration pins domains and then reduces S_{switch} . Thus, the S_{pos} of ceramics at $y = 9$ decreases.

Figure 6 shows the unipolar S - E curves for the KNNT-0.055BZ + 0.03Zr + y Mn ceramics. All the ceramics have been poled under a DC field of 3 kV/mm for 30 min and then were placed in air for 2 days. Unfortunately, the S - E curves of ceramics at $y = 5$ cannot be tested well as shown in Fig. S3 in the ESM, because a large number of mobile oxygen vacancies occur in ceramics and its k is relatively low. It can be observed that the MnO dopant can improve the unipolar strain of the poled KNNT-0.055BZ + 0.03Zr + y Mn ceramics. The ceramics at $y = 8$ show an optimum unipolar strain in Fig. 6. The d_{33}^* is calculated by the equation $d_{33}^* = S_{\text{max}}/E_{\text{max}}$. The electric field dependence of d_{33}^* is shown in the insets of Fig. 6. For d_{33}^* of all ceramics, the d_{33}^* value reaches a maximum under an applied electric field ($E = 20$ kV/cm). This means that the KNNT-0.055BZ + 0.03Zr + y Mn system can be induced to form high d_{33}^* under low electric field. In Fig. 6, under applying an electric field ($E = 20$ kV/cm), the ceramics

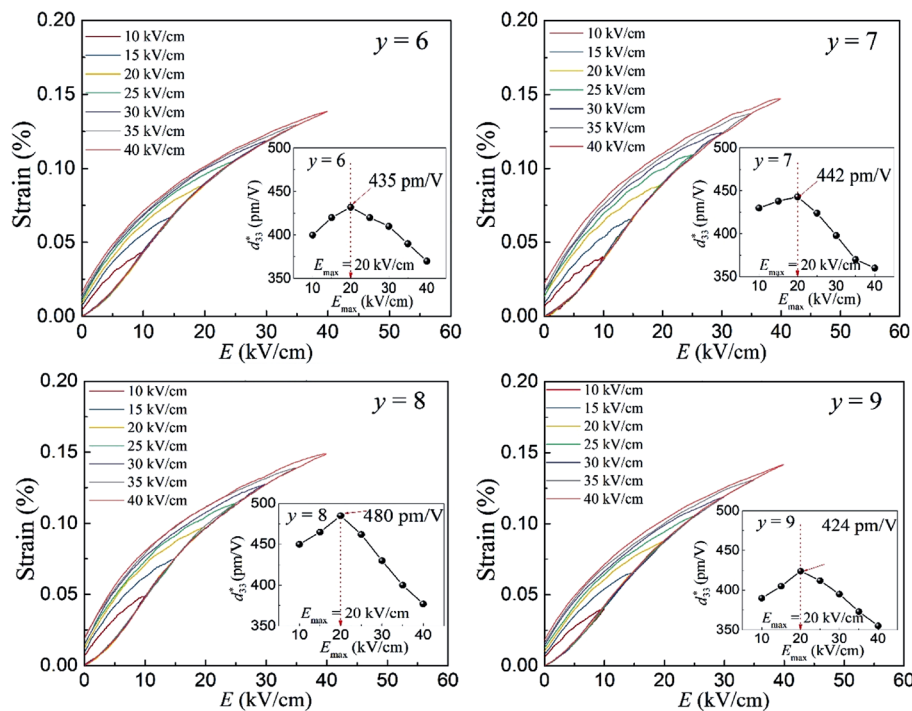


Fig. 6 Unipolar S – E curves and d_{33}^* for the poled KNNT–0.055BZ + 0.03Zr + y Mn ceramics.

at $y = 8$ show a maximal d_{33}^* value (480 pm/V).

Figure 7(a) shows the temperature dependence of d_{33}^* for the poled KNNT–0.055BZ + 0.03Zr + y Mn ceramics under $E = 20$ kV/cm. When the d_{33}^* value is lower than 90% of the room-temperature d_{33}^* value, the corresponding temperature point (T_e) is used to evaluate the temperature stability. In Fig. 7(a), it can be observed that the T_e increases from 145 to 158 °C and then decreases to 150 °C. Figure 7(b) shows the temperature dependence of representative unipolar strain curves for the poled KNNT–0.055BZ + 0.03Zr + y Mn ceramics. MnO dopant can not only improve the piezoelectric strain, but also improve its temperature stability. Reducing alkali metal volatilization by decreasing T_{sinter} is responsible for the piezoelectric properties and temperature stability. For KNN-based piezoelectric ceramics, it is usually difficult to improve simultaneously piezoelectric properties and its temperature stability, because polymorphic phase boundary (PPB) shows very high-temperature sensitivity. Piezoelectric properties and temperature stability of the poled KNNT–0.055BZ + 0.03Zr + y Mn ceramics at $y = 8$ are improved.

Figure 8 shows unipolar S – E field curves of the poled KNNT–0.055BZ + 0.03Zr + y Mn ceramics before and after 10^4 , 10^5 , and 10^6 unipolar fatigue cycles. It can be observed that strain of ceramics after

unipolar fatigue cycles occurs degradation. Here, the degree (β) of d_{33}^* degradation is calculated as shown in Eq. (9).

$$\beta(\%) = d_{33}^*(N) \times 100 / d_{33}^*(10^0) \quad (9)$$

where $d_{33}^*(10^0)$ refers to the inverse piezoelectric coefficient of ceramics before fatigued cycles. $d_{33}^*(N)$ refers to the inverse piezoelectric coefficient of ceramics after fatigued cycles. N refers to the unipolar fatigue cycles (10^4 , 10^5 , or 10^6). All ceramics before fatigued cycles are poled at 30 kV/cm and aged 2 days. The d_{33}^* of ceramics reduces with increasing unipolar fatigue cycles from 10^4 to 10^6 . In Fig. 8, it can be observed that all ceramics after 10^6 unipolar fatigue cycles show excellent anti-fatigue property ($\beta > 94\%$). It suggests that KNNT–0.055BZ + 0.03Zr + y Mn ceramics have great potential for application in the future due to the excellent anti-fatigue property. When the ceramics are fatigued cycles 10^6 , the β values of all ceramics are approximate. The change of the β value is not very obvious, which should be attributed to the synergistic effect of two possible situations. The first one is the excellent fatigue resistant can be interpreted by the decrease of oxygen vacancy concentration [31]. However, the ceramics at $y = 8$ possess the lowest oxygen vacancy concentration and it should show optimum anti-fatigue property, namely the highest β

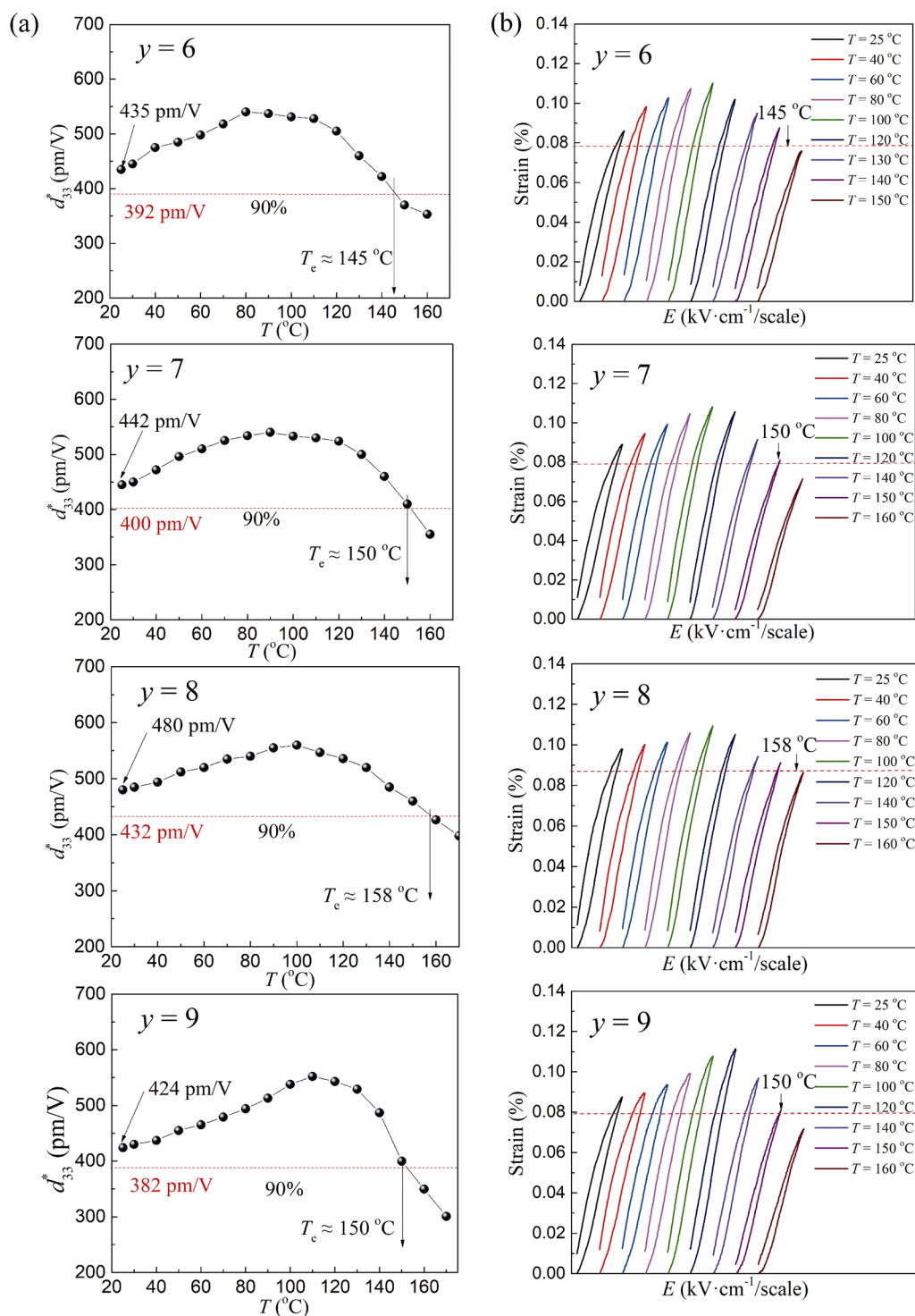


Fig. 7 (a) Temperature dependence of d_{33}^* and (b) temperature dependence of representative unipolar strain curves for the poled KNNT–0.055BZ + 0.03Zr + y Mn ceramics.

value. At $y = 6–9$, the ceramics do not show an increase of β value, or even a slight decrease. This is due to another reason that it should be closely related to the grain size of the ceramics. The mechanical stress during the fatigue process induces microstructure damage that

results in the unipolar strain degradation [32]. The mechanical strength of ceramics with coarse grain is usually lower than that of fine grains. The ceramics at $y = 8$ possess maximal average grain size ($\sim 1.65 \mu\text{m}$) as shown in Fig. 1. We consider that microstructure

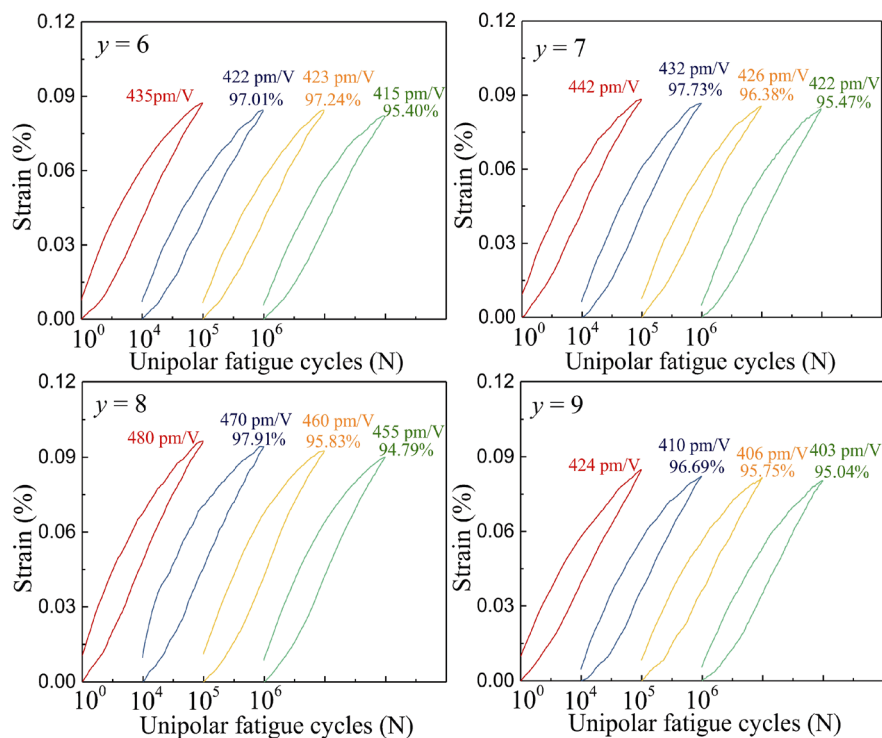


Fig. 8 Unipolar S - E curves of the poled KNNT-0.055BZ + 0.03Zr + y Mn ceramics before and after 10^4 , 10^5 , and 10^6 unipolar fatigue cycles.

damage in fatigued ceramics at $y = 8$ should be the largest. Thus, under the synergistic effect of reduced oxygen vacancies due to reduced volatilization and increased grain size, the β value basically does not change.

4 Conclusions

Lead-free KNNT-0.055BZ + 0.03Zr + y Mn ceramics sintered in reducing atmosphere (p_{O_2} : 10^{-12} - 10^{-11} MPa) were prepared by conventional solid-state reaction methods. MnO dopant increases grain size at $y = 5$ -8 due to strong lattice distortion and then decreases at $y = 9$ due to much $Mn_4Nb_2O_9$ accumulated at the grain boundary. In the regulation of oxygen vacancies in KNN-based ceramics, the effect of reducing T_{sinter} is stronger than that of Mn ion substitution in B-site. The MnO dopant as an excellent sintering aid can effectively reduce the volatilization of alkali metals via reducing the T_{sinter} . Oxygen vacancies caused by the volatilization of alkali metals account for a large proportion of oxygen vacancies in the KNNT-0.055BZ + 0.03Zr + y Mn ceramics. The oxygen vacancy concentration decreases at $y = 5$ -8 and then increases at $y = 9$. The decrease of grain size is beneficial to the increase of Schottky

barrier. MnO dopant can improve the anti-reduction properties. The KNNT-0.055BZ + 0.03Zr + y Mn ceramics at $y = 6$ -9 show excellent anti-fatigue of unipolar piezoelectric strain ($\beta > 94\%$) under the synergistic effect of reduced oxygen vacancies due to reduced volatilization and increased grain size. Piezoelectric properties and temperature stability of the KNNT-0.055BZ + 0.03Zr ceramics sintered in reducing atmosphere are synchronously improved by MnO dopant. The ceramics at $y = 8$ show optimum piezoelectric strain ($d_{33}^* = 480$ pm/V at 20 kV/cm). Its d_{33}^* reaches up to ~ 480 pm/V at low driving electric field $E = 20$ kV/cm at room temperature, and its temperature stability of d_{33}^* reaches 158 °C. This provides a good lead-free material matrix for the preparation of multilayer nickel electrode piezoelectric actuators.

Acknowledgements

The work was supported by the National Postdoctoral Program for Innovative Talents (Grant No. BX20190158), National Natural Science Foundation of China (Grant Nos. 52032005 and 51672148), and the Shuimu Tsinghua Scholar.

Electronic Supplementary Material

Supplementary material is available in the online version of this article at <https://doi.org/10.1007/s40145-021-0475-0>.

References

- [1] Tao H, Wu H, Liu Y, *et al.* Ultrahigh performance in lead-free piezoceramics utilizing a relaxor slush polar state with multiphase coexistence. *J Am Chem Soc* 2019, **141**: 13987–13994.
- [2] Kobayashi K, Doshida Y, Mizuno Y, *et al.* Possibility of cofiring a nickel inner electrode in a $(\text{Na}_{0.5}\text{K}_{0.5})\text{NbO}_3\text{-LiF}$ piezoelectric actuator. *Jpn J Appl Phys* 2013, **52**: 09KD07.
- [3] Fisher JG, Kang SJL. Microstructural changes in $(\text{K}_{0.5}\text{Na}_{0.5})\text{NbO}_3$ ceramics sintered in various atmospheres. *J Eur Ceram Soc* 2009, **29**: 2581–2588.
- [4] Vendrell X, García JE, Rubio-Marcos F, *et al.* Exploring different sintering atmospheres to reduce nonlinear response of modified KNN piezoceramics. *J Eur Ceram Soc* 2013, **33**: 825–831.
- [5] Teranishi S, Suzuki M, Noguchi Y, *et al.* Giant strain in lead-free $(\text{Bi}_{0.5}\text{Na}_{0.5})\text{TiO}_3$ -based single crystals. *Appl Phys Lett* 2008, **92**: 182905.
- [6] Qiao XS, Chen XM, Lian HL, *et al.* Microstructure and electrical properties of nonstoichiometric $0.94(\text{Na}_{0.5}\text{Bi}_{0.5+x})\text{TiO}_3\text{-}0.06\text{BaTiO}_3$ lead-free ceramics. *J Am Ceram Soc* 2016, **99**: 198–205.
- [7] Saiful Islam M. Ionic transport in ABO_3 perovskite oxides: A computer modelling tour. *J Mater Chem* 2000, **10**: 1027–1038.
- [8] Kobayashi K, Doshida Y, Mizuno Y, *et al.* A route forwards to narrow the performance gap between PZT and lead-free piezoelectric ceramic with low oxygen partial pressure processed $(\text{Na}_{0.5}\text{K}_{0.5})\text{NbO}_3$. *J Am Ceram Soc* 2012, **95**: 2928–2933.
- [9] Watanabe Y, Sumida K, Yamada S, *et al.* Effect of Mn-doping on the piezoelectric properties of $(\text{K}_{0.5}\text{Na}_{0.5})(\text{Nb}_{0.67}\text{Ta}_{0.33})\text{O}_3$ lead-free ceramics. *Jpn J Appl Phys* 2008, **47**: 3556–3558.
- [10] Mgbemere HE, Herber RP, Schneider GA. Effect of MnO_2 on the dielectric and piezoelectric properties of alkaline niobate based lead free piezoelectric ceramics. *J Eur Ceram Soc* 2009, **29**: 1729–1733.
- [11] Lin DM, Kwok KW, Tian HY, *et al.* Phase transitions and electrical properties of $(\text{Na}_{1-x}\text{K}_x)(\text{Nb}_{1-y}\text{Sb}_y)\text{O}_3$ lead-free piezoelectric ceramics with a MnO_2 sintering aid. *J Am Ceram Soc* 2007, **90**: 1458–1462.
- [12] Kizaki Y, Noguchi Y, Miyayama M. Defect control for low leakage current in $\text{K}_{0.5}\text{Na}_{0.5}\text{NbO}_3$ single crystals. *Appl Phys Lett* 2006, **89**: 142910.
- [13] Noguchi Y, Miyayama M. Effect of Mn doping on the leakage current and polarization properties in $\text{K}_{0.14}\text{Na}_{0.86}\text{NbO}_3$ ferroelectric single crystals. *J Ceram Soc Jpn* 2010, **118**: 711–716.
- [14] Kawada S, Hayashi H, Ishii H, *et al.* Potassium sodium niobate-based lead-free piezoelectric multilayer ceramics Co-fired with nickel electrodes. *Materials* 2015, **8**: 7423–7438.
- [15] Moulder JF, Stickle WF, Sobol PE, *et al.* *Handbook of X-ray Photoelectron Spectroscopy: A Reference Book of Standard Spectra for Identification and Interpretation of XPS Data*. Minnesota (USA): Physical Electronics, 1992.
- [16] Shannon RD. Revised effective ionic radii and systematic studies of interatomic distances in halides and chalcogenides. *Acta Cryst A* 1976, **32**: 751–767.
- [17] Rafiq MA, Tkach A, Costa ME, *et al.* Defects and charge transport in Mn-doped $\text{K}_{0.5}\text{Na}_{0.5}\text{NbO}_3$ ceramics. *Phys Chem Chem Phys* 2015, **17**: 24403–24411.
- [18] Li JF, Wang K, Zhu FY, *et al.* $(\text{K},\text{Na})\text{NbO}_3$ -based lead-free piezoceramics: Fundamental aspects, processing technologies, and remaining challenges. *J Am Ceram Soc* 2013, **96**: 3677–3696.
- [19] Zhang BY, Wu JG, Wang XP, *et al.* Rhombohedral–orthorhombic phase coexistence and electrical properties of Ta and BaZrO_3 co-modified $(\text{K},\text{Na})\text{NbO}_3$ lead-free ceramics. *Curr Appl Phys* 2013, **13**: 1647–1650.
- [20] Cheng XX, Zhou DX, Fu QY, *et al.* Effect of reoxidation annealing on the PTCR behaviour of multilayer Nb^{5+} -doped BaTiO_3 ceramics with a Ni internal electrode. *J Phys D: Appl Phys* 2012, **45**: 385306.
- [21] Niimi H, Mihara K, Sakabe Y, *et al.* Influence of Ba/Ti ratio on the positive temperature coefficient of resistivity characteristics of Ca-doped semiconducting BaTiO_3 fired in reducing atmosphere and reoxidized in air. *J Am Ceram Soc* 2007, **90**: 1817–1821.
- [22] Gao C, Fu QY, Zhou DX, *et al.* Nanocrystalline semiconducting donor-doped BaTiO_3 ceramics for laminated PTC thermistor. *J Eur Ceram Soc* 2017, **37**: 1523–1528.
- [23] Sun Y, Liu HX, Hao H, *et al.* Effect of oxygen vacancy on electrical property of acceptor doped $\text{BaTiO}_3\text{-Na}_{0.5}\text{Bi}_{0.5}\text{TiO}_3\text{-Nb}_2\text{O}_5$ X8R systems. *J Am Ceram Soc* 2016, **99**: 3067–3073.
- [24] Yoon SH, Randall CA, Hur KH. Effect of acceptor (Mg) concentration on the resistance degradation behavior in acceptor (Mg)-doped BaTiO_3 bulk ceramics: I. impedance analysis. *J Am Ceram Soc* 2009, **92**: 1758–1765.
- [25] Robels U, Arlt G. Domain wall clamping in ferroelectrics by orientation of defects. *J Appl Phys* 1993, **73**: 3454–3460.
- [26] Jin L, Li F, Zhang SJ. Decoding the fingerprint of ferroelectric loops: Comprehension of the material properties and structures. *J Am Ceram Soc* 2014, **97**: 1–27.
- [27] Zhao ZH, Dai YJ, Li XL, *et al.* The evolution mechanism of defect dipoles and high strain in MnO_2 -doped KNN lead-free ceramics. *Appl Phys Lett* 2016, **108**: 172906.
- [28] Feng ZY, Ren XB. Aging effect and large recoverable electrostrain in Mn-doped KNbO_3 -based ferroelectrics. *Appl Phys Lett* 2007, **91**: 032904.

- [29] Ge HY, Hou YD, Rao X, *et al.* The investigation of depoling mechanism of densified KNbO₃ piezoelectric ceramic. *Appl Phys Lett* 2011, **99**: 032905.
- [30] Fu J, Zuo RZ. Giant electrostrains accompanying the evolution of a relaxor behavior in Bi(Mg,Ti)O₃–PbZrO₃–PbTiO₃ ferroelectric ceramics. *Acta Mater* 2013, **61**: 3687–3694.
- [31] Li P, Chen XQ, Wang FF, *et al.* Microscopic insight into electric fatigue resistance and thermally stable piezoelectric properties of (K,Na)NbO₃-based ceramics. *ACS Appl Mater Interfaces* 2018, **10**: 28772–28779.
- [32] Luo ZH, Glaum J, Granzow T, *et al.* Bipolar and unipolar fatigue of ferroelectric BNT-based lead-free piezoceramics. *J Am Ceram Soc* 2011, **94**: 529–535.

Open Access This article is licensed under a Creative Commons Attribution 4.0 International License, which permits use, sharing, adaptation, distribution and reproduction in any medium or format, as long as you give appropriate credit to the original author(s) and the source, provide a link to the Creative Commons licence, and indicate if changes were made.

The images or other third party material in this article are included in the article's Creative Commons licence, unless indicated otherwise in a credit line to the material. If material is not included in the article's Creative Commons licence and your intended use is not permitted by statutory regulation or exceeds the permitted use, you will need to obtain permission directly from the copyright holder.

To view a copy of this licence, visit <http://creativecommons.org/licenses/by/4.0/>.